Title
Focusing metasurface quantum-cascade laser with a near diffraction-limited beam.

Journal
Optics Express, 24(21)

ISSN
1094-4087

Authors
Xu, Luyao
Chen, Daguan
Itoh, Tatsuo
et al.

Publication Date
2016-10-17

DOI
10.1364/oe.24.024117

Peer reviewed

Focusing metasurface quantum-cascade laser with a near diffraction-limited beam

LUYAO XU,[1,2] DAGUAN CHEN,[1] TATSUO ITOH,[1] JOHN L. RENO,[3] AND BENJAMIN S. WILLIAMS[1,2,*]

[1]*Department of Electrical Engineering, University of California, Los Angeles, CA 90095, USA*
[2]*California NanoSystems Institute, University of California, Los Angeles, CA 90095, USA*
[3]*Sandia National Laboratories, Center of Integrated Nanotechnologies, MS 1303, Albuquerque, NM 87185, USA*
[*]*bswilliams@ucla.edu*

Abstract: A terahertz vertical-external-cavity surface-emitting-laser (VECSEL) is demonstrated using an active focusing reflectarray metasurface based on quantum-cascade gain material. The focusing effect enables a hemispherical cavity with flat optics, which exhibits higher geometric stability than a plano-plano cavity and a directive and circular near-diffraction limited Gaussian beam with M^2 beam parameter as low as 1.3 and brightness of 1.86×10^6 $\mathrm{Wsr^{-1}m^{-2}}$. This work initiates the potential of leveraging inhomogeneous metasurface and reflectarray designs to achieve high-power and high-brightness terahertz quantum-cascade VECSELs.

OCIS codes: (140.5965) Semiconductor lasers, quantum cascade; (140.7270) Vertical emitting lasers; (160.3918) Metamaterials.

References and links

1. J. Huang and J. A. Encinar, *Reflectarray Antennas* (Wiley-IEEE, 2007).
2. Y. Rahmat-Samii, "Reflector antennas," in *Antenna Engineering Handbook*, J. L. Volakis, ed. (McGraw-Hill Companies, 2007).
3. D. Berry, R. Malech, and W. Kennedy, "The reflectarray antenna," IEEE Trans. Antenn. Propag. **11**(6), 645–651 (1963).
4. D. M. Pozar and T. A. Metzler, "Analysis of a reflectarray antenna using microstrip patches of variable size," Electron. Lett. **29**(8), 657–658 (1993).
5. T. Niu, W. Withayachumnankul, B. S. Y. Ung, H. Menekse, M. Bhaskaran, S. Sriram, and C. Fumeaux, "Experimental demonstration of reflectarray antennas at terahertz frequencies," Opt. Express **21**(3), 2875–2889 (2013).
6. J. Ginn, B. Lail, J. Alda, and G. Boreman, "Planar infrared binary phase reflectarray," Opt. Lett. **33**(8), 779–781 (2008).
7. J. C. Ginn, B. A. Lail, and G. D. Boreman, "Phase Characterization of Reflectarray Elements at Infrared," IEEE Trans. Antenn. Propag. **55**(11), 2989–2993 (2007).
8. N. Yu, P. Genevet, F. Aieta, M. A. Kats, R. Blanchard, G. Aoust, J. P. Tetienne, Z. Gaburro, and F. Capasso, "Flat Optics: Controlling Wavefronts With Optical Antenna Metasurfaces," IEEE J. Sel. Top. Quantum Electron. **19**(3), 4700423 (2013).
9. P. Genevet and F. Capasso, "Holographic optical metasurfaces: a review of current progress," Rep. Prog. Phys. **78**(2), 024401 (2015).
10. A. A. Tavallaee, P. W. C. Hon, Q.-S. Chen, T. Itoh, and B. S. Williams, "Active terahertz quantum-cascade composite right/left handed metamaterial," Appl. Phys. Lett. **102**(2), 021103 (2013).
11. N. Meinzer, M. Ruther, S. Linden, C. M. Soukoulis, G. Khitrova, J. Hendrickson, J. D. Olitzky, H. M. Gibbs, and M. Wegener, "Arrays of Ag split-ring resonators coupled to InGaAs single-quantum-well gain," Opt. Express **18**(23), 24140–24151 (2010).
12. E. Plum, V. A. Fedotov, P. Kuo, D. P. Tsai, and N. I. Zheludev, "Towards the lasing spaser: controlling metamaterial optical response with semiconductor quantum dots," Opt. Express **17**(10), 8548–8551 (2009).
13. S. Xiao, V. P. Drachev, A. V. Kildishev, X. Ni, U. K. Chettiar, H.-K. Yuan, and V. M. Shalaev, "Loss-free and active optical negative-index metamaterials," Nature **466**(7307), 735–738 (2010).
14. L. Xu, C. A. Curwen, P. W. C. Hon, Q.-S. Chen, T. Itoh, and B. S. Williams, "Metasurface external cavity laser," Appl. Phys. Lett. **107**(22), 221105 (2015).
15. J. B. Khurgin, "How to deal with the loss in plasmonics and metamaterials," Nat. Nanotechnol. **10**(1), 2–6 (2015).

16. B. S. Williams, S. Kumar, H. Callebaut, Q. Hu, and J. L. Reno, "Terahertz quantum-cascade laser at $l \sim 100$ mm using metal waveguide for mode confinement," Appl. Phys. Lett. **83**(11), 2124 (2003).
17. P. H. Siegel, "Terahertz technology," IEEE Trans. Microw. Theory Tech. **50**(3), 910–928 (2002).
18. M. Kuznetsov, F. Hakimi, R. Sprague, and A. Mooradian, "High-Power (0.5-W CW) Diode-Pumped Vertical-External-Cavity Surface-Emitting Semiconductor Lasers with Circular TEM Beams," IEEE Photonics Technol. Lett. **9**(8), 1063–1065 (1997).
19. A. C. Tropper, H. D. Foreman, A. Garnache, K. G. Wilcox, and S. H. Hoogland, "Vertical-external-cavity semiconductor lasers," J. Phys. D Appl. Phys. **37**(9), R75–R85 (2004).
20. M. I. Amanti, M. Fischer, G. Scalari, M. Beck, and J. Faist, "Low-divergence single-mode terahertz quantum cascade laser," Nat. Photonics **3**(10), 586–590 (2009).
21. T.-Y. Kao, J. L. Reno, and Q. Hu, "Phase-locked laser arrays through global antenna mutual coupling," Nat. Photonics **10**(8), 541–546 (2016).
22. G. Xu, R. Colombelli, S. P. Khanna, A. Belarouci, X. Letartre, L. Li, E. H. Linfield, A. G. Davies, H. E. Beere, and D. A. Ritchie, "Efficient power extraction in surface-emitting semiconductor lasers using graded photonic heterostructures," Nat. Commun. **3**, 952 (2012).
23. C. Wu, S. Khanal, J. L. Reno, and S. Kumar, "Terahertz plasmonic laser radiating in an ultra-narrow beam," Optica **3**(7), 734–740 (2016).
24. R. Densing, A. Erstling, M. Gogolbwski, H.-P. Gemund, G. Lundershausen, and A. Gatesman, "Effective far infrared laser operation with mesh couplers," Infrared Phys. **33**(3), 219–226 (1992).
25. S. T. Shanahan and N. R. Heckenberg, "Transmission line model of substrate effects on capacitive mesh couplers," Appl. Opt. **20**(23), 4019–4023 (1981).
26. A. A. Tavallaee, B. S. Williams, P. W. C. Hon, T. Itoh, and Q.-S. Chen, "Terahertz quantum-cascade laser with active leaky-wave antenna," Appl. Phys. Lett. **99**(14), 141115 (2011).
27. P. W. C. Hon, A. A. Tavallaee, Q.-S. Chen, B. S. Williams, and T. Itoh, "Radiation Model for Terahertz Transmission-Line Metamaterial Quantum-Cascade Lasers," IEEE Trans. Terahertz Sci. Technol. **2**(3), 323–332 (2012).
28. L. Li, L. Chen, J. Zhu, J. Freeman, P. Dean, A. Valavanis, A. G. Davies, and E. H. Linfield, "Terahertz quantum cascade lasers with >1 W output powers," Electron. Lett. **50**(4), 309–311 (2014).
29. A. G. Fox and T. Li, "Resonant Modes in a Maser Interferometer," Bell Syst. Tech. J. **40**(2), 453–488 (1961).
30. A. E. Siegman, M. W. Sasnett, and T. F. Johnston, "Choice of clip levels for beam width measurements using knife-edge techniques," IEEE J. Quantum Electron. **27**(4), 1098–1104 (1991).
31. H. Richter, N. Rothbart, and H.-w. Hübers, "Characterizing the beam properties of terahertz quantum-cascade lasers," J. Infrared Millim. THz Waves **35**, 686–698 (2014).
32. " International Organization for Standardization, document no. ISO 11146, Lasers and laser-related equipment – Test methods for laser beam parameters – Beam width, divergence, angle and beam propagation factor " (1999).
33. T. Y. Kao, Q. Hu, J. L. Reno, L. Wang, J. Zhang, and Z. Wang, "Perfectly phase-matched third-order distributed feedback terahertz quantum-cascade lasers," Opt. Lett. **37**(11), 2070–2072 (2012).

1. Introduction

The ability to engineer the phase of scattered light from planar surfaces is a powerful tool for beam engineering, which allows one to replace bulky optical components with thin and flat equivalents. This concept was introduced in the microwave regime in the form of the reflectarray antenna, often used to replace space-fed parabolic reflectors [1–3]. In its most common realization, a reflectarray comprises arrays of resonant patch antennas, which are used to engineer a spatially dependent reflection phase by varying a critical dimension of the patch; reflectarray lenses of this type have been demonstrated in the mm-wave, THz, and mid-IR ranges [4–7]. The concept has been further generalized across the infrared and visible spectrum, with both metallic, plasmonic, and dielectric antennas types used to create a huge variety of reflectarray and transmitarray metasurface optical components – including lenses for focusing and imaging [8, 9]. However, there has been relatively little experimental work on integrating gain into the metasurface itself, whether simply for mitigating losses, or for implementing new laser concepts [10–14]. This is understandable, since in the infrared and visible the metallic/plasmonic elements that make up many metasurfaces are prohibitively lossy [15]. However, the situation is quite favorable in the terahertz frequency range, where metals have sufficiently modest losses that quantum-cascade (QC) lasers can effectively use sub-wavelength metallic waveguides [16].

In this work we propose and demonstrate an inhomogeneous active reflectarray metasurface which acts as a focusing element by mimicking a parabolic concave mirror; this is done by using a spatially inhomogeneous metasurface design which imposes a phase shift

on the reflected wave that increases quadratically as the distance from the center. Furthermore, in our demonstration the reflectarray antenna elements are loaded with QC active materials; when electrically biased the metasurface amplifies the reflected beam as it focuses. In conjunction with a flat output coupler (OC) reflector, we used the focusing metasurface to create a QC vertical-external-cavity surface-emitting-laser (VECSEL) with a hemispherical cavity, as shown in Fig. 1(b). Thanks to the focusing effect, we observe a significant improvement in cavity stability and output beam pattern compared to a non-focusing metasurface configuration [14]. This directly benefits the development of high-power THz sources with excellent beam patterns, which are desired for various applications such as THz heterodyne detection in astrophysics and space science, biological and medical imaging/spectroscopy, and non-destructive sensing [17].

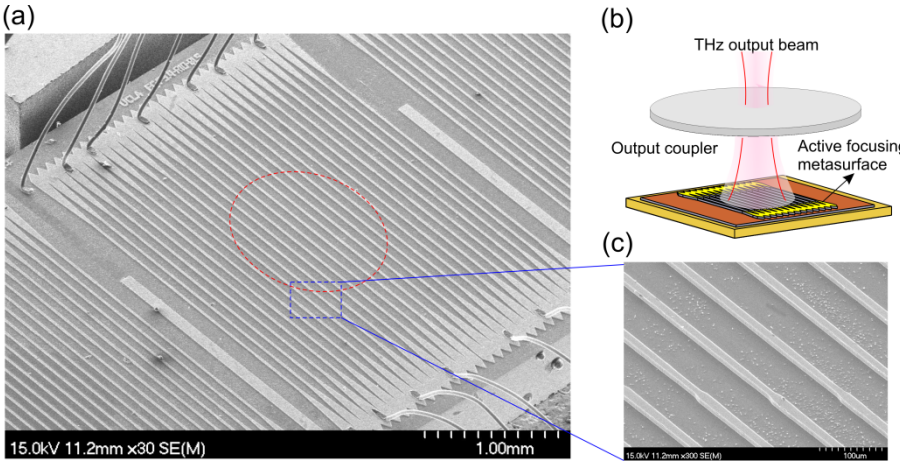

Fig. 1. (a) SEM image of a 2 × 2 mm^2 active focusing metasurface with wire bonds. Only the part of ridges within the red dashed circle (1 mm diameter) are electrically biased; the area outside has a SiO_2 insulation layer between the top metal contact and the QC material. (b) Schematic for a THz QC-VECSEL based on an active focusing metasurface acting as an amplifying concave mirror. (c) Zoom-in SEM image of a part of the focusing metasurface showing the ridge width variation along and across the ridges.

The foundation of this work rests upon our recent demonstration of the first QC-VECSEL [14]. VECSELs are widely used in the visible and near-IR for to obtain high output power in a diffraction-limited beam [18, 19]. The critical element in the QC-VECSEL is a reflectarray metasurface made up of a periodic array of identical low-Q sub-cavities. Each sub-cavity is a metal-metal waveguide of width w loaded with electrically biased QC active material, so that incident THz radiation is reflected and amplified. The active metasurface was paired with a flat output coupler reflector to form a plano-plano Fabry-Pérot (FP) VECSEL cavity. In contrast to most other on-chip cavity engineering approaches for THz QC-lasers [20–23], for a QC-VECSEL the output beam pattern is determined by the VECSEL cavity rather than the sub-cavities. Furthermore, by proper choice of the OC reflectivity, the output power can be maximized. From the perspective of design, the QC-VECSEL approach disentangles the issue of beam engineering from output power optimization. The first prototype QC-VECSEL was built upon a plano-plano cavity at the edge of geometric stability, and therefore was intolerant to misalignment due to walk-off losses. The natural solution would be to use a concave mirror OC to form a stable hemispherical cavity. However, such components are not readily available in the THz range; planar OC components are far more convenient and can be easily manufactured using lithographic techniques [24, 25]. In this work, we present an active focusing reflectarray metasurface, which replaces our original uniform metasurface made up of identical sub-cavity elements, and acts as an amplifying concave mirror to form a stable hemispherical cavity.

2. Design

The focusing metasurface is composed of an array of inhomogeneous metal-metal waveguide ridges, as shown in Figs. 1(a) and 1(c), which have the QC active material sandwiched between the top metal contact and metal ground plane. Each metal-metal waveguide is intended to operate around its TM_{01} mode cutoff as an elongated patch antenna [26, 27]; normally incident radiation is coupled to the QC active material, where it is amplified and re-radiated back to free-space. The resonance condition is approximately determined by $w \approx \lambda_0/2n$, (where n is the index of the QC semiconductor material), although there is a weak dependence on the period Λ. The normal-to-ground electric field polarization of TM_{01} mode satisfies the "polarization selection rule" for intersubband transitions. Each ridge is tapered to the passive and lossy wire bonding areas on both ends, which helps to suppress lasing of the fundamental waveguide mode.

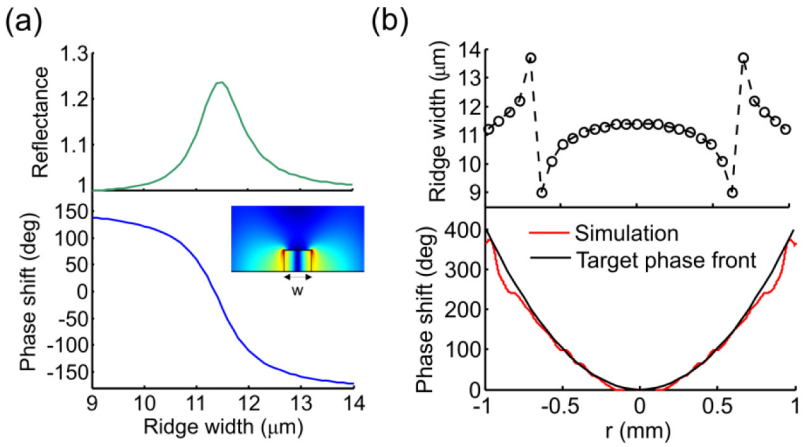

Fig. 2. (a) Simulated reflectance (top) and reflection phase shift (bottom) versus ridge width for a metal-metal waveguide array with period of 70 μm, with 30 cm^{-1} bulk gain assumed in the QC gain medium. Inset is the electric field amplitude profile of the excited TM_{01} mode in the reflection simulation. (b) Designed ridge width distribution for a focusing metasurface of R = 10 mm at 3.4 THz (top), and simulated phase front of reflected wave with a plane wave incident on it, in comparison with the target parabolic phase front (bottom).

The focusing effect is achieved by spatially modulating the ridge width both along and transverse to the ridges (see Fig. 1(c)). Because of the resonance characteristics of metal-metal waveguides, at a fixed frequency nearly 2π change in reflection phase can be obtained by altering the ridge width w around the resonance condition. Figure 2(a) shows that a phase change of 311° is achieved by varying w from 9 μm to 14 μm. The designed 2 × 2 mm^2 focusing metasurface is made up of 29 tapered metal-metal waveguide ridges spaced with a period of Λ = 70 μm, which is chosen to be smaller than the free-space wavelength λ_0 to suppress Bragg scattering. The ridge width w at the metasurface center is chosen to match the resonant frequency of the element to intersubband gain spectrum peak. The modulation in ridge width is designed to achieve the target parabolic phase profile (for paraxial focusing) of $2\pi r^2/R\lambda_0$, where r is the radial distance to the metasurface center and R is the effective radius of curvature (i.e. twice the desired focal length). As an example, a focusing metasurface designed with R = 10 mm at 3.4 THz has its transverse ridge width distribution through the center as shown in Fig. 2(b). Its focusing effect is verified by numerically simulating the reflection of a plane wave from it in 2D and confirmed by the result that the simulated phase profile shown in Fig. 2(b) matches with the target parabolic profile (Comsol Multiphysics 4.4). The fact that the reflectance is highest near the resonance frequency provides an approximate "self-selection" of the correct frequency to obtain the desired phase

profile. We designed focusing metasurfaces with R = 10 and 20 mm for four different frequencies covering 3.2–3.5 THz to overlap with the QC material bulk gain peak (designs labeled M3.2, M3.3, M3.4, M3.5).

3. Fabrication

The active region design used in this work is a phonon depopulation design very similar to that described in [28]. It was grown via molecular beam epitaxy in the GaAs/$Al_{0.15}Ga_{0.85}As$ material system (wafer number VB0739). The fabrication of the metasurfaces followed the standard steps for making metal-metal waveguides. The 10 μm-thick active QC layer was bonded to a receiving GaAs wafer via Cu-Cu thermocompression bonding. Then 200 nm of SiO_2 was deposited and patterned in order to isolate the taper, wire-bonding area, and part of waveguide array area from the top metal contact so that only the center circular area of 1 mm diameter is electrically biased (see Fig. 1(a) red circled area). Finally a Ti/Au/Ni metal layer was evaporated and lifted off to provide top metallization and self-aligned etch mask for the subsequent Chlorine-based dry etching to define the ridges, followed by the removal of Ni layer. Along with the fabrication of focusing metasurfaces, several uniform metasurfaces similar to those described in [14] were also fabricated, with the ridge width varying from 11 μm to 12.5 μm and the center circular bias area of 1.5 mm diameter.

The experimental configuration for the VECSEL is shown in Fig. 3(a), where the metasurface is attached to a Cu submount using In solder, and mounted inside a cryostat. The cryostat has a 3-mm thick silicon window that acts as an intracavity etalon filter. The cavity length is ~9 mm – the shortest length allowed by the experimental setup. As the cavity length is increased, the VECSEL peak power drops and the threshold current increases, mainly due to the higher air absorption loss and diffraction loss (see Appendix A). The output coupler used here is either an inductive metal mesh on a 100 μm-thick quartz substrate (OC1) or a capacitive metal mesh on a 75 μm-thick quartz substrate (OC2), whose transmittance is measured to vary between 10 and 24% for the former and 40–60% for the latter, depending on the frequency within 3.2–3.5 THz due to the substrate's etalon effect [25].

4. Results

Upon testing, it was immediately apparent that the focusing designs were easier to align and more tolerant of misalignment compared to uniform metasurface designs. This was quantified by first optimizing the alignment of the cavity to achieve parallelism, and then intentionally introducing angular misalignment in either the x or y axis represented by tilt angles δ_x and δ_x respectively (see Fig. 3(a)). A host of pulsed optical power-current-voltage (P-I-V) curves (see Fig. 3(b)) were measured for increased tilt angles in both axes for QC-VECSELs built upon three metasurfaces: focusing ones of R = 10 mm and 20 mm, and a uniform metasurface. The pulsed P-I-V measurements were conducted with 0.25% overall duty cycle (500 ns-long pulses repeated at 10 kHz, modulated by a slow 5 Hz pulse train with lock-in detection). To make a fair comparison, for each device the measured change in threshold current density J_{th} is plotted normalized to J_{th} measured at optimum alignment (see Fig. 3(c)). The threshold current increases with the tilt angle in both axes in a modest manner for the two focusing metasurface QC-VECSELs – devices still lase even with 4° misalignment. In contrast, the uniform metasurface exhibits a more dramatic rise in J_{th} with misalignment, and ceases to lase entirely for misalignments greater than 3.5°. This is the case even though the uniform metasurface has a larger circular biased area of 1.5 mm diameter and consumes more current. We conclude that the focusing effect significantly reduces the cavity's sensitivity to misalignment, as is expected for the hemispherical Gaussian resonator. The experimental result matches the trend of our simulated results, in which modified Fox-and-Li cavity calculation is used to estimate the threshold bulk gain g_{th} for each QC-VECSEL to lase at different misaligned angles [14, 29]. The threshold bulk gain is found by using a root finder algorithm to find the value of the metasurface reflectivity for which the computed round-trip

cavity loss is zero. The angular misalignment is introduced as a linear shift of the OC's reflection phase. The calculation results reveal a slower trend of threshold bulk gain increase with misalignment for the two focusing metasurfaces than for the uniform one, as shown in the top part of Fig. 3(c). Because not all loss mechanisms are included in this simulation, it should only be used to identify the trend in threshold current density.

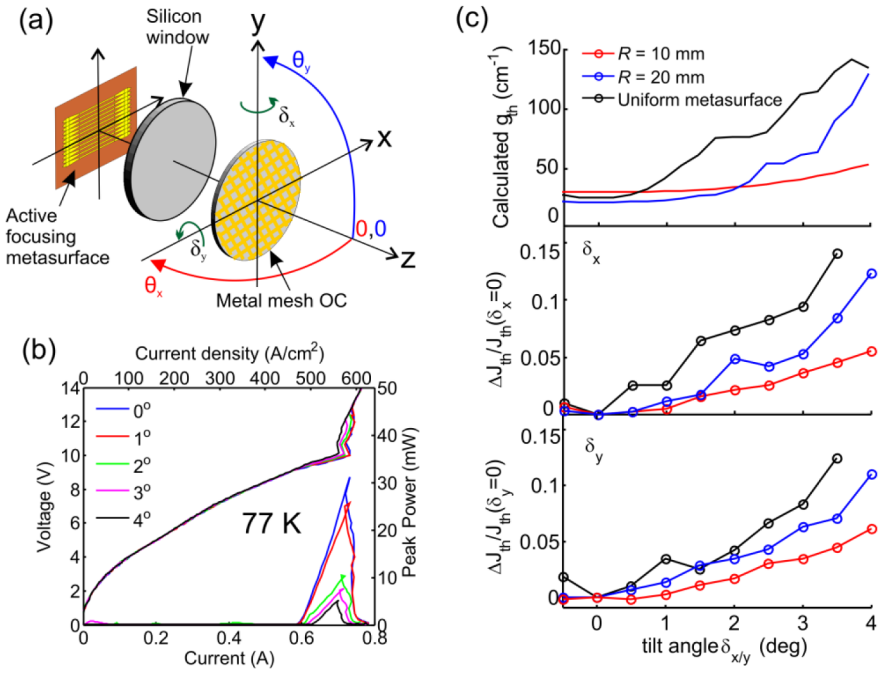

Fig. 3. (a) Experimental configuration of a focusing metasurface QC-VECSEL. The tilt angle $\delta_{x/y}$ indicates the degree of OC tilting around y/x axis from the perfectly aligned position, as the green arrows show. (b) Pulsed *P-I-V* curves at 77 K for different δ_y (with $\delta_x = 0$) for a R = 10 mm focusing metasurface (M3.4). (c) The measured threshold current density change ratio with respect to J_{th} at perfect alignment with δ_x and δ_y for QC-VECSELs based upon three different metasurfaces: R = 10 mm and 20 mm with 1 mm diameter circular bias area, and a uniform metasurface with 1.5 mm diameter circular bias area. The solid lines in the top part are the calculated threshold bulk gain g_{th} change with the tilt angle δ_y.

High power output and slope efficiency are demonstrated from the focusing metasurface QC-VECSELs. All four separate metasurfaces designed for four frequencies covering 3.2-3.5 THz were observed to lase, with the one designed for 3.4 THz (M3.4) showing the best power performance. At perfect alignment and 77 K, the R = 10 mm metasurface QC-VECSEL designed for 3.4 THz generates a peak power of 46 mW with the slope efficiency dP/dI = 413 mW/A when paired with OC2, and 31 mW peak power with dP/dI = 227 mW/A with OC1, *P-I-V* curves of which are plotted in Fig. 4(a). At 6 K, the pulsed peak power increases to 78 mW, with dP/dI = 572 mW/A with OC2 and a peak wall-plug efficiency reaching ~1.15%. Continuous wave (cw) lasing is achieved at 6 K with peak power of 40 mW, dP/dI = 339 mW/A, and wall-plug efficiency of 0.6%. (see Fig. 4(b)). The power is measured using a pyroelectric detector and calibrated using a Thomas-Keating THz absolute power meter with 100% collection efficiency, given directive beam pattern. For a comparison, the 77-K *P-I-V* of a uniform metasurface QC-VECSEL is measured and shows dP/dI = 234 mW/A when paired with OC1 (*P-I-V* curve not shown). The output power drops dramatically when this uniform metasurface is paired with OC2. Even though the focusing metasurface is designed with a smaller circular bias area (1 mm diameter) than the uniform metasurface (1.5 mm diameter), higher efficiency performance is obtained from the focusing metasurface

VECSEL, with the slope efficiency among the best reported numbers so far from a THz QC-laser. The smaller biased area of the focusing design has reduces the total current consumption and benefits cw operation. Further reduction of the biased area may help to obtain cw performance at higher temperature (i.e. > 77 K).

The lasing spectra for four separate focusing metasurface VECSELs designed for 3.2–3.5 THz at 77 K are shown in Fig. 4(c). The spectra are generally close to the designed metasurface frequencies, which is primarily determined by the ridge width at the metasurface center. All lased in single-mode over their entire bias range. This is attributed to the etalon filter effect of the cryostat window, which causes the cavity loss to vary rapidly with frequency with minima separated by the free spectral range of ~13 GHz. This effect, in combination with the limited bandwidth of the metasurface reflective gain, and the QC material gain lineshape, strongly favors single-mode operation.

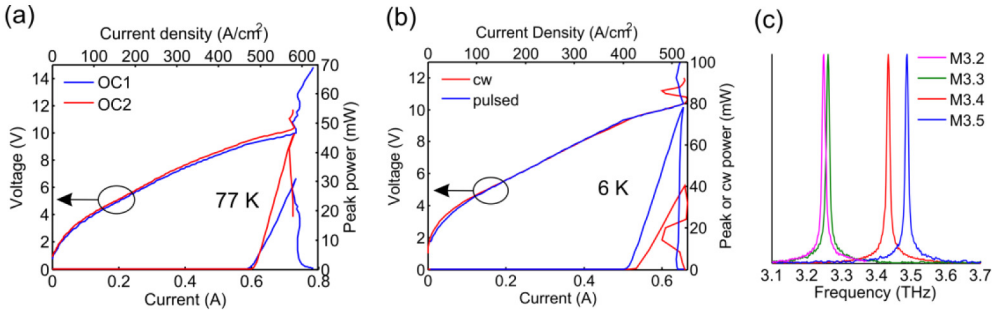

Fig. 4. (a) Pulsed *P-I-V* curves for the R = 10 mm focusing metasurface QC-VECSEL designed for 3.4 THz, paired with OC1 and OC2 respectively at 77 K. (b) Pulsed and cw *P-I-V* curves for the QC-VECSEL composed of the R = 10 mm focusing metasurface and OC2 at 6 K. (c) Lasing spectra measured using a Nicolet FTIR using 0.25 cm^{-1} resolution for QC-VECSELs based on four focusing metasurfaces M3.2, M3.3, M3.4, and M3.5 paired with either OC1 or OC2 at 77 K.

The benefit of the focusing metasurface can also be seen by looking at the beam quality. The far-field beam at 77 K is measured as shown in Fig. 3(a) using a 2-axis spherical scanning pyroelectric detector. Beams from the focusing QC-VECSELs both exhibit a narrower and more circular near-Gaussian beam profile than the beam pattern reported in [14] from a uniform metasurface. As shown in Figs. 5(a) and 5(b), the QC-VECSEL on R = 20 mm focusing metasurface produces a beam with 3.5° × 3.6° FWHM angular divergence, and the QC-VECSEL with the R = 10 mm metasurface produces a beam with 4.8° × 4.3° divergence. This agrees with the expected divergence behavior of Gaussian modes in hemispherical resonators – the smaller value of R produces a smaller spot on the output coupler, with consequent faster divergence in the far-field. The beam is well fit by a Gaussian intensity profile at least down to –25 dB, and in some cases down to –40 dB.

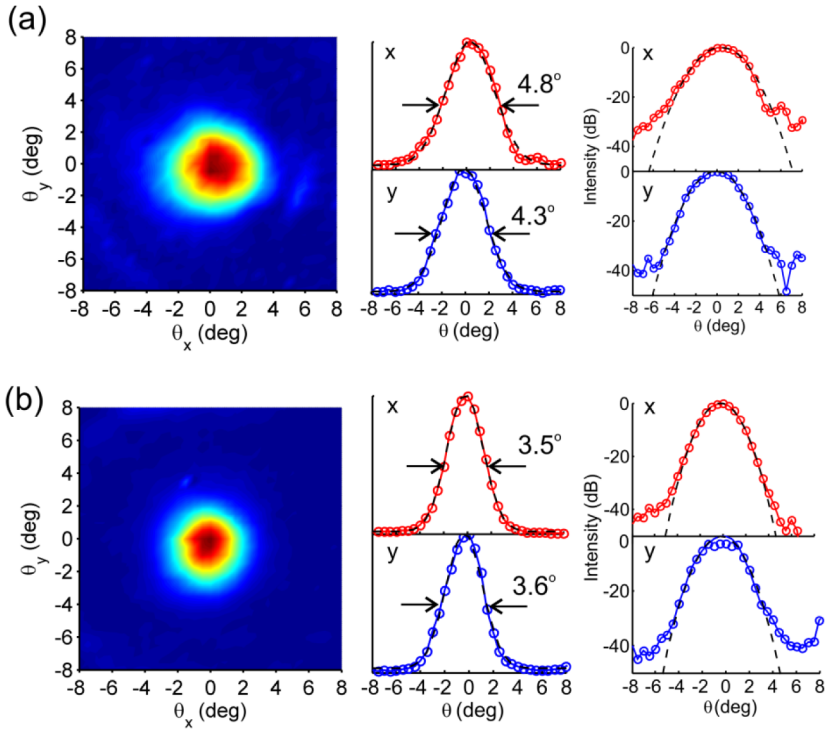

Fig. 5. (a) The measured beam pattern from a focusing metasurface QC-VECSEL with R = 10 mm. (b) The measured beam pattern from a focusing metasurface QC-VECSEL with R = 20 mm. The angular resolution in measurement is 0.5°. Black dashed lines are Gaussian curve fits to the 1D beam cuts through the beam center. 1D beams cuts are also plotted dB scale. Beams are measured at 77 K.

To further assess the beam quality, the beam propagation factor M^2 is measured using a knife edge method through the focus of the beam along the propagation direction [30]. The M^2 factor is the ratio of the angle of divergence of a laser beam to that of a fundamental Gaussian TEM_{00} mode with the same beam waist diameter; it has a value of unity for a fundamental Gaussian beam [31]. Following the standard procedures detailed in [32], a value of M^2 = 1.3 is measured in both the x and y directions for R = 20 mm metasurface QC-VECSEL, which is the best reported M^2 factor directly from a THz QC-laser based on metal-metal waveguide geometry with no spatial filtering [33]. The beam waist evolution along the optical axis is shown in Fig. 6, with parameter fitting results. The peak power associated with this beam is 27 mW at 77 K, which leads to a high value of brightness $B_r = 1.86 \times 10^6$ $Wsr^{-1}m^{-2}$ given by $B_r = P/(M_x^2 M_y^2 \lambda^2)$, where P is the output power. The M^2 value for R = 10 mm metasurface QC-VECSEL with OC2 is measured to be 2.2 and 2.5 in x and y directions respectively, with the output power of 46 mW and $B_r = 1.07 \times 10^6$ $Wsr^{-1}m^{-2}$. The slight beam degradation may be due to the stronger diffraction occurring for such a cavity where the cavity length is closer to the focusing curvature radius. We note that only providing electrical bias to the center circular area with diameter of 1 mm is important in achieving high beam quality. By pumping only the center of the metasurface, the fundamental Gaussian mode exhibits the highest overlap, and is selectively excited. Also, even for the R = 10 mm design, the ridge widths w are relatively uniform within the center biased region (see Fig. 2(b)), which limits the spectral broadening of the gain due to metasurface inhomogeneity. Several focusing devices were tested where the bias area was larger (1.5 mm diameter); these VECSELs exhibited beams with large sidelobes, indicating the presence of higher-order

Hermite-Gaussian components in the cavity mode. The long data collection times prevented beam pattern measurements at 6 K and in cw mode.

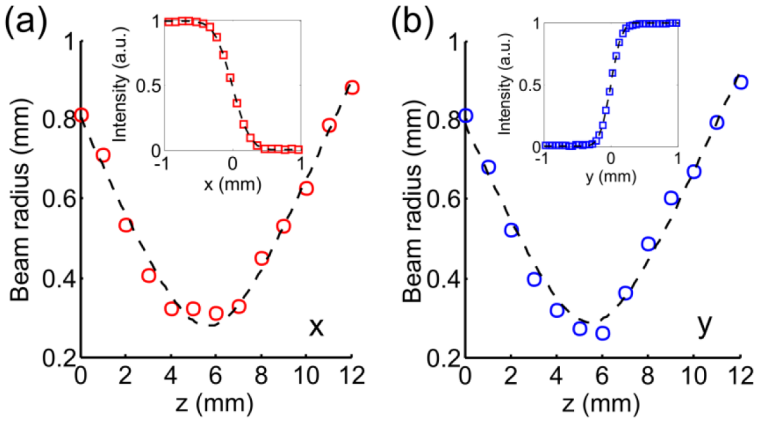

Fig. 6. M^2 factor measurement results for the output beam directly from a focusing metasurface QC-VECSEL with R = 20 mm. The beam radius is measured along the optical axis (z axis) in both x and y direction after being focused by a TPX lens of 50-mm focal length which is placed 17 cm away from the VECSEL, and is represented by red and blue circles in (a) and (b), with the curve fitting results plotted in black dashed line. The inset shows the knife-edge measurement raw data at beam waist position with curve fitting shown in black dashed curve.

5. Conclusion

In this work, amplifying and focusing reflectarray metasurfaces have been shown to be a powerful tool to make high-performance THz QC-VECSELs. The inhomogeneous focusing metasurface significantly improves the cavity stability, beam pattern quality, and power efficiency of a QC-VECSEL, in comparison to a uniform metasurface. The observed slope efficiency numbers (with the best at 572 mW/A) are larger than reported from other single- and multi-mode THz QC-lasers [20–22, 28]. The generated beams demonstrate a near diffraction limited beam quality (M^2 as low as 1.3) form with very narrow divergence and high brightness. Our observed beams have comparable or smaller divergence angles than the best reported results for THz QC-lasers, including end-fire 3rd order DFB cavities (6° × 11°) [20, 33], antenna-feedback DFB cavities (4° × 4°) [23], and phased-locked QC-laser arrays through antenna mutual coupling (~10° × 10°) [21].

This work demonstrates the promise of inhomogeneous reflectarray metasurface design to provide improved performance to QC-VECSELs. Specifically, nonuniform spatial phase allows one to engineer focusing devices for compact planar QC-VECSEL cavities. Non-uniform gain (via control of the current injection area) allows one to ensure selective pumping of the desired mode, and to keep the total injection current modest as is necessary for cw performance. The versatile nature of the reflectarray concept allows one to integrate advanced functionality onto the planar gain chip; this is highly advantageous in the THz region, where many basic optical components are not readily available. From the designer's perspective, the metasurface QC-VECSEL approach embodies the modular design concept; it separates the design and optimization of active metasurface, output coupling component, and VECSEL cavity characteristics, which eases the design flow and facilitates improvement/addition of modules.

Appendix A: Supplementary experimental data

In order to provide a comparison with the data in Fig. 4(a), the pulsed-mode *P-I-V* of a M3.3 R=20 mm focusing metasurface VECSEL at 77 K, paired with output coupler 1 (OC1) in is shown in Fig. 7(a). The peak power reaches 27 mW, a slope efficiency of 238 mW/A is

measured, and the device operates in single-mode over its entire bias range. The beam measurements of Fig. 5(b) and Fig. 6 are associated with operation of this device at its maximum output power point. The peak power drops when it is paired with OC2 (data not shown).

Shown in Fig. 7(b) is the pulsed mode *P-I-V* of the uniform metasurface VECSEL at 77 K paired with OC1. The metasurface is designed to provide peak gain at 3.3 THz, i.e. the ridges are 12 μm wide. The peak power is 69 mW, larger than the focusing devices using OC1 due to its larger bias area (1.5 mm diameter), but the slope efficiency is 234 mW/A, very similar to that of the focusing designs. Single-mode lasing is exhibited across the entire bias range at 3.36 THz. The peak power drops dramatically to approximately 10 mW (not shown) when this uniform metasurface is paired with OC2.

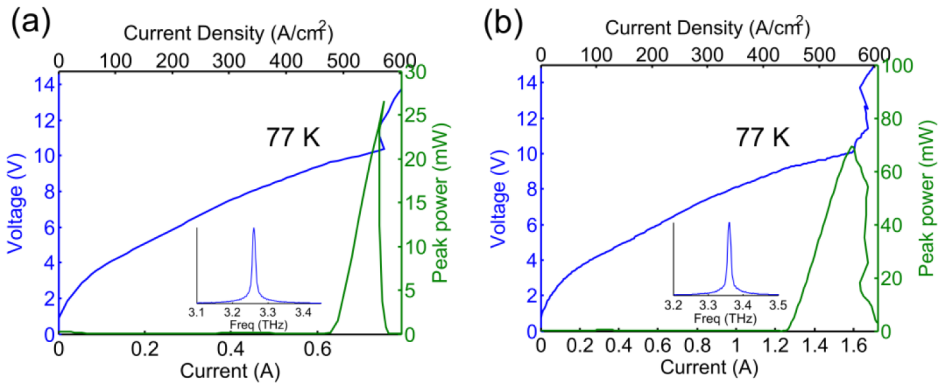

Fig. 7. (a) Pulsed *P-I-V* characteristics for the M3.3 $R = 20$ mm focusing metasurface VECSEL with OC1 at 77 K, and 1 mm bias area diameter. (b) Pulsed *P-I-V* characteristics for the uniform M3.3 metasurface VECSEL with OC1 at 77 K. Insets in each show the lasing spectrum.

The pulsed mode *P-I-Vs* of the $R = 20$ mm focusing metasurface VECSEL paired with OC1 at 77 K are measured for different cavity lengths increased from 9 mm to 17 mm, as shown in Fig. 8. We were unable to obtain cavity lengths smaller than 9 mm due to space restrictions of the cryostat and device mounts. As the cavity length is increased, both the peak power and slope efficiency drop, and the threshold current density increases. These indicate an increase in cavity loss due to larger absorption in the atmosphere, as well as higher diffraction loss due to the broader mode profile on the metasurface.

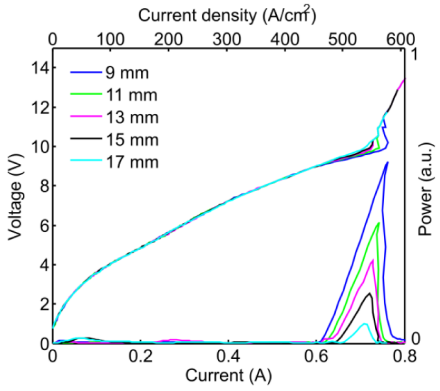

Fig. 8. *P-I-V* curves for $R = 20$ mm focusing metasurface VECSEL with different cavity lengths.

Appendix B: Fox and Li modeling of cavity

We use the iterative Fox-and-Li approach (adapted for QC-VECSELs as detailed in [14]) to calculate the intracavity mode profiles. To evaluate the impact of the nonuniform distribution of reflectance on the metasurface focusing effect, we calculated and compared the cavity mode profiles and far-field beam patterns for four cases: ideal Gaussian cavity with a smooth parabolic phase for R = 10 mm and uniform unity reflectance, the actual R = 10 mm focusing metasurface design with phase profile modulated by the ridge width distribution transverse to the ridge array and a "fictitious" uniform reflectance, and finally the actual R = 10 mm focusing metasurface design with a nonuniform reflectance distribution for 30 cm^{-1} and 60 cm^{-1} gain within the active material. Fig. 9(a) shows the associated metasurface reflectivity magnitude and phase distributions. The nonuniform reflectance data was obtained by using finite-element simulation to obtain the metasurface reflectance as a function of ridge width. It is assumed that sub-cavity elements within the center 1 mm are biased to produce a bulk gain coefficient of 30 – 60 cm^{-1} within the active material, and the other elements outside are unbiased so that they are lossy. The range of gain values considered leads might correspond to operation with different output couplers; i.e. a more transmissive output coupler will require larger threshold gain to oscillate. Since the metasurface resonance is approximately Lorentzian in lineshape, the modulation of the ridge width to produce the desired phase profile also produces a spatially varying gain profile at a fixed frequency, whose variation depends upon the total cavity loss. Fig. 9(b) shows the calculated intensity far-field beam pattern, as well as the modal profiles on the metasurface and the output coupler, for each of the four cases. The results show that the field distributions are very similar. Therefore we believe that the nonuniform reflectance distribution has only a minor effect on the focusing metasurface cavity mode.

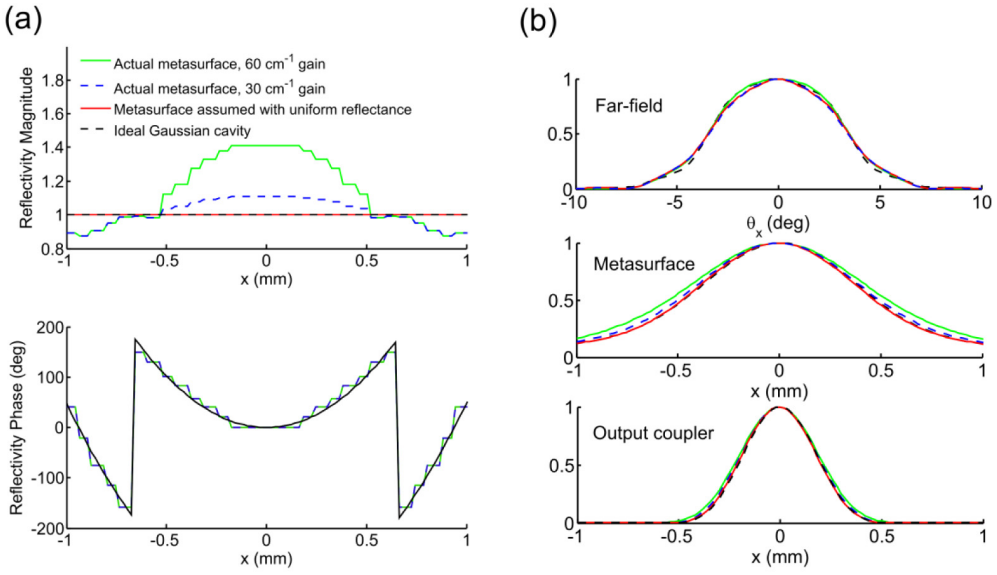

Fig. 9. (a) Reflectivity magnitude and phase distributions for the four calculation cases. (b) Calculated far-field beam patterns, cavity mode intensity profiles on metasurface and OC for the four cases.

Funding

National Science Foundation (NSF) (1150071, 1407711), National Aeronautics and Space Administration (NASA) (NNX16AC73G).

Acknowledgments

The authors thank C. Curwen for valuable conversations. Microfabrication was performed at the UCLA Nanoelectronics Research Facility, and wire bonding was performed at the UCLA Center for High Frequency Electronics. We thank the JPL SWAT Group for use of its Thomas Keating power meter. This work was performed, in part, at the Center for Integrated Nanotechnologies, an Office of Science User Facility operated for the U.S. Department of Energy (DOE) Office of Science. Sandia National Laboratories is a multi-program laboratory managed and operated by Sandia Corporation, a wholly owned subsidiary of Lockheed Martin Corporation, for the U.S. Department of Energy's National Nuclear Security Administration under contract DE-AC04-94AL85000.